J. Am. Soc. Mass Spectrom. (2018) 29:2402–2412
DOI: 10.1007/s13361-018-2053-4

RESEARCH ARTICLE

Comparison of Peptide Ion Conformers Arising from Non-Helical and Helical Peptides Using Ion Mobility Spectrometry and Gas-Phase Hydrogen/Deuterium Exchange

Ahmad Kiani Karanji,[1] Mahdiar Khakinejad,[2] Samaneh Ghassabi Kondalaji,[2] Sandra N. Majuta,[1] Kushani Attanayake,[1] Stephen J. Valentine[1]

[1]Department of Chemistry, West Virginia University, Morgantown, WV 26506, USA
[2]*Present Address:* Department of Biophysics, Johns Hopkins University, Baltimore, MD 21218, USA

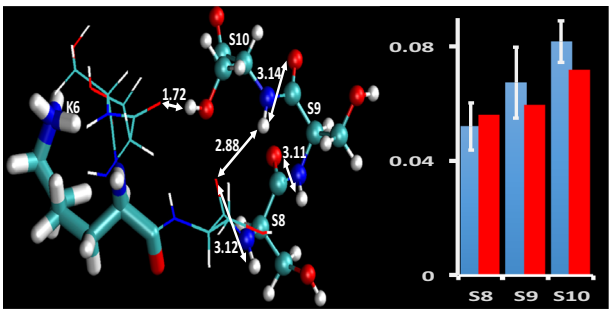

Abstract. The dominant gas-phase conformer of $[M+3H]^{3+}$ ions of the model peptide acetyl-PSSSSKSSSSKSSSSKSSSSK has been examined with ion mobility spectrometry (IMS), gas-phase hydrogen deuterium exchange (HDX), and mass spectrometry (MS) techniques. The $[M+3H]^{3+}$ peptide ions are observed predominantly as a relatively compact conformer type. Upon subjecting these ions to electron transfer dissociation (ETD), the level of protection for each amino acid residue in the peptide sequence is assessed. The overall per-residue deuterium uptake is observed to be relatively more efficient for the neutral residues than for the model peptide acetyl-PAAAAKAAAAKAAAAKAAAAK. In comparison, the N-terminal and C-terminal regions of the serine peptide show greater relative protection compared with interior residues. Molecular dynamics (MD) simulations have been used to generate candidate structures for collision cross section and HDX reactivity matching. Hydrogen accessibility scoring (HAS) for select structural candidates from MD simulations has been used to suggest conformer types that could contribute to the observed HDX patterns. The results are discussed with respect to recent studies employing extensive MD simulations of gas-phase structure establishment of a peptide system.

Keywords: Ion mobility spectrometry, Hydrogen deuterium exchange, Tandem mass spectrometry, Molecular dynamics simulations

Received: 7 May 2018/Revised: 17 July 2018/Accepted: 3 August 2018/Published Online: 15 October 2018

Introduction

Since the discovery of the structure of the α-helix in polypeptides [1], significant research has been devoted to determining factors that affect the formation of elements of secondary structure and in particular those effecting helix formation [2]. Initial efforts, boosted by the expanding available protein structure data, focused on the relationship between the presence of α-helices and the frequency of occurrence of specific amino acid residues [3–7]. Shortly later, Chou and Fasman proposed a method for predicting this secondary structure element using amino acid sequence information [8]. Over the next several decades, interest in helix structure prediction progressed to the point where a relatively high degree of accuracy was obtained [9, 10]. This progress coincided with efforts to refine helix propensities of the individual amino acid residues [2, 11, 12] and the concept has even been extended to structure destabilization imparted by D-amino acid residues [13, 14].

The rapid increase in the number of experimentally determined protein structures over the last three decades [15, 16] has

Electronic supplementary material The online version of this article (https://doi.org/10.1007/s13361-018-2053-4) contains supplementary material, which is available to authorized users.

Correspondence to: Stephen Valentine;
e-mail: stephen.valentine@mail.wvu.edu

significantly enabled protein structure prediction capabilities. Perhaps, the simplest conception is to use sequence homology based on comparisons to known structures to infer structural elements for proteins of interest [17–19]. Over the years, other computational techniques have advanced significantly and protein structure prediction efforts can currently be grouped into those using ab initio methods (or ab initio-guided approaches) and template-based methods (fold recognition and threading, comparative modeling) [20]. Currently, protein structure prediction remains a highly active and rapidly evolving area of research [21–23].

A challenge in the characterization of polypeptide structure is species that have been designated as intrinsically disordered [24–26]. Although efforts have been developed for predicting unstructured regions of proteins [27, 28], recent developments regarding the nature of species classified as intrinsically disordered have called into question whether or not structural assessments are possible. One area of interest is the study of peptide structure. For example, the peptide bradykinin was examined by NMR many years ago and only a small portion of the molecule was assigned to a β-turn structural type [29]. Recent experiments that employed ion mobility spectrometry (IMS) combined with mass spectrometry (MS) have shed some light on the inability of solution-phase measurements to determine prevailing structural motifs for peptides; for bradykinin, these experiments revealed the presence of multiple, co-existing solution structures [30, 31]. Although the exact relationship of gas-phase structures to antecedent solution states is still under investigation, such efforts suggested that gas-phase analyses could provide insight into the various structures of polypeptides that exist in solution. Interestingly, extending the approach has suggested the presence of multiple protein structures for species for which well-defined native conformations predominate [32].

Results from the early IMS-MS experiments lead to questions regarding the degree to which elements of secondary structure are preserved in the gas-phase for such dynamic systems and whether or not solution structures can be derived from high-quality gas-phase structures. To study this, recent experiments have examined the conformations of $[M+3H]^{3+}$ ions of the model peptide acetyl-PAAAAKAAAAKAAAAKAAAAK (hereafter referred to as the A-containing peptide) using a combination of IMS-MS and gas-phase hydrogen/deuterium exchange (HDX) measurements and molecular modeling techniques [33–35]. This peptide was selected because of its relatively large propensity to form a helix in solution [2, 36, 37]. In general, studies suggested that the presence of multiple conformer types of varying degree of helicity can contribute to the $[M+3H]^{3+}$ ion conformers that were studied [33]. In many respects, this work was similar in nature to early efforts aimed at designing gas-phase peptide ion structure [38] as well as studies that have characterized peptide structural motifs with gas-phase HDX [39, 40].

The present work examines the $[M+3H]^{3+}$ ions of a the model peptide acetyl-PSSSSKSSSSKSSSSKSSSSK (hereafter referred to as the S-containing peptide). This peptide has been designed to exhibit less helical propensity in solution [2]. Indeed, because the hydroxyl oxygen of serine (S) can hydrogen bond with the carbonyl oxygen of the third residue, S is known to destabilize α-helix structure [41]. Additionally, regions of high S density are associated with helix-breaking structure [42]. The model peptide was also designed because of the potential to experience a different process of gas-phase conformation establishment when compared with the previously studied A-containing peptide. Previous work has suggested that the non-polar A residues may strongly associate with the apolar vacuum environment during the final stages of ESI [35, 43]; it may be expected that the S residues will more strongly favor solvent interaction during the final stages of ESI. These differences offer the opportunity to compare the ion structure types formed by very different solution conformers and possibly by different processes of gas-phase conformer establishment.

Overall, ion collision cross section values are nearly the same compared with the A-containing peptide. However, because the S-containing peptide has a larger molecular weight, one may conclude the overall structure is more compact. Additionally, there are significant differences in the relative accessibility of exchange sites of terminal and middle amino acid residues with the latter being more accessible to the S-containing peptide. These characteristics are discussed below using structures obtained from simulated annealing to help provide insight into relative accessibility. By providing information about gas-phase ion conformer establishment from different solution states, these efforts may help to enhance protein structure prediction tools in the future. Finally, this work adds to the growing repertoire of studies that employ IMS-MS, gas-phase HDX, and/or MD simulation techniques for peptide/protein ion structure characterization [44–54].

Experimental

Sample Preparation

The model peptide acetyl-PSSSSKSSSSKSSSSKSSSSK (97.3% purity) was purchased from GenScript (Piscataway, NJ, USA) and used without further purification. To prepare the 1 mg/mL stock solution, the peptide was dissolved in the appropriate amount of Milli-Q water. The stock solution was then diluted 10-fold with a 100 mM solution of ammonium acetate in water to prepare the ESI solutions. This solution was infused (0.5 μL/min) through a pulled-tipped capillary which was biased ~ + 2200 V relative to the entrance of the hybrid IMS-MS instrument.

IMS-HDX-MS Measurements

For the ion mobility measurements conducted here, a dual-gate drift tube similar to others described in the literature was used [55, 56]. The details of the drift time (t_D) and MS measurements have been described in detail previously [57, 58]. Briefly, for this study, ions generated by ESI were periodically (50 Hz) pulsed into a ~ 1-m-long drift tube that was filled with ~2.5 Torr of 300 K helium buffer gas. For the dual ion gate

approach, the second gate was set to transmit at specific delay times in order to record mobility-resolved mass spectra. This delay time was scanned (200-μs increments) across the mobility distribution of the $[M+3H]^{3+}$ ions. Mass spectra were recorded by a linear ion trap (LTQ Velos; ThermoScientific, San Jose, CA, USA) instrument. A mass-to-charge (*m/z*) range of 400 to 1000 was employed. For each t_D, increment mass spectra were recorded for 0.5 min. For mobility selection, the second ion gate was set to transmit for 200 μs.

The HDX measurements conducted here are modeled after foundational work in which the reactivities of different biomolecular ions were examined upon reaction with gaseous deuterating reagent [59–66]. For HDX measurements, ~0.02 Torr of D_2O was added to the buffer gas. With the addition of D_2O, the t_D distributions shifted to longer times as shown in Fig. 1. Therefore, for the tandem MS (MS/MS) measurements, the delay times were scanned across the t_D distributions obtained when employing D_2O to determine the mobility selection time corresponding with the dominant, compact conformer type for the $[M+3H]^{3+}$ ions. As it was desired to examine the HDX behavior of the dominant, most compact ion conformer type, mobility selection was initiated 200 μs prior to the peak maximum time point in order to minimize contamination from larger ions (Fig. 1).

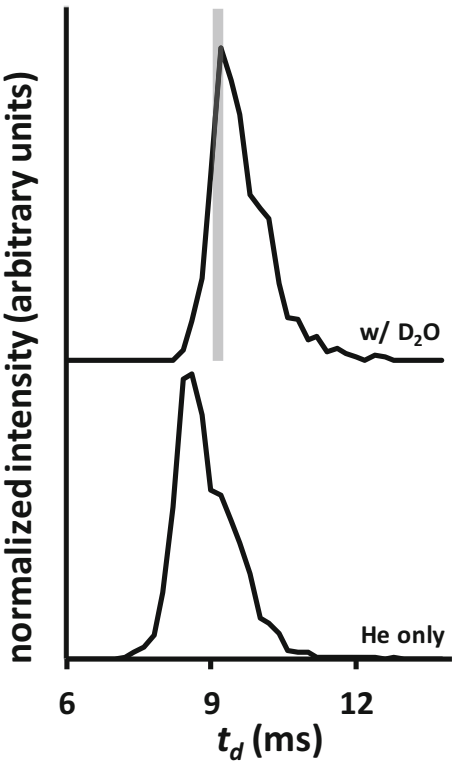

Figure 1. t_D distributions for the $[M+3H]^{3+}$ ions of the model peptide acetyl-PSSSSKSSSSKSSSSKSSSSK. The bottom and top traces show the distributions obtained in the absence of D_2O and after the introduction of ~0.02 Torr D_2O. For both distributions, a delay step time of 200 μs was used and each mobility-resolved spectrum was collected for 0.5 min. Integration of the isotopic envelope for the $[M+3H]^{3+}$ ions at each delay time setting provided the intensity values for the distributions. The distributions have been normalized to show relative intensities. The gray bar in the top trace shows the typical mobility selection time and width

Peptide Ion Dissociation by ETD and Per-residue Deuterium Uptake Calculations

The MS/MS analyses described here have also been influenced by foundational work demonstrating the utility of MS/MS to determine deuterium uptake from gas- and solution-phase experiments [67–69]. Briefly, mobility-selected $[M+3H]^{3+}$ ions were subjected to electron transfer dissociation (ETD) [70] to determine the per-residue deuterium incorporation as described previously [57, 71]. To perform ETD measurements, mobility-selected ions were isolated by *m/z* and the ion injection time was maintained at 200 ms (5 microscans). Because ETD did not generate a number of lower *m/z* ions, the deuterium uptake value for each residue was obtained using both *z*- and *c*-type ions. The per-residue deuterium uptake values for the fragment ions were obtained by first subtracting the average mass of the fragment ions obtained in the absence of D_2O from the average mass of those generated upon using D_2O reagent gas. For the triplicate measurements, the amount of deuterium incorporated in each residue was calculated by subtracting the deuterium uptake values of the appropriate adjacent fragment ions. Here, it is noted that mass spectrometer conditions including all focusing optics were maintained at conditions that have been shown to not induce deuterium scrambling [72].

Molecular Dynamics Simulations

Details regarding the in vacuo molecular dynamics (MD) simulations can also be found in the prior, related work [73]. Briefly, the initial structures of the $[M+3H]^{3+}$ ions for simulated annealing were generated using the Visual Molecular Dynamics (VMD). The CHARMM36 force field was employed for structural parameterization. All of the parameters were defined in this force field. The CNEU patch in the top_all36_prot topology file were used to protonate the C-terminal K residue resulting in a +1 formal charge. The LSN patch was used to protonate the more N-terminal K residues. Acetyl groups were attached to the N-terminus portion of the P residue by using the ACP patch. Five thousand steps of geometry and energy minimization were carried out using the Nanoscale Molecular Dynamics (NAMD) software suite for the $[M+3H]^{3+}$ peptide ions with charge arrangements of K(6)-K(11)-K(16), K(6)-K(11)-K(21), K(6)-K(16)-K(21), and K(11)-K(16)-K(21). Then, the structures were subjected to cyclic simulated annealing (SA) for conformational space sampling. For SA runs (timestep of 1 fs), the Berendsen temperature coupling algorithm was used. For the SA algorithm, the temperature of the in vacuo system was suddenly increased to 1010 K over 10 steps. The heated structure was maintained at that temperature for 40 ps and then cooled to a lower temperature (10 K) over two different timescales (40 and 1200 ps). The annealed structures were subsequently energy minimized

to 0 K to generate candidate structures. The energy minimized structure of each cycle was imported as the starting point for the next heating-cooling cycle. Each minimized structure was gradually heated to 300 K and equilibrated. The structures then undergo 5 ns of MD simulations with no non-bonded cutoffs for long-range interactions while the temperature was constant. The Mobcal software suite [74] was used to calculate theoretical collision cross-section values using the trajectory method [75].

Hydrogen Accessibility Scoring and HDX Kinetics Modeling

Hydrogen accessibility scoring (HAS) scores were calculated for in silico structures with matching collision cross sections. Two candidate structures which contained CCS values matching experimental measurements were selected for discussion. The selection was based on a first-pass examination of HAS scores for which one ion structure displayed increased proximity of charge sites to middle residues while the other displayed less access to these residues (see discussion below) as is suggested to be required by the "relay" mechanism for HDX [76]. Hydrogen accessibility was computed as described previously [77] where each carbonyl site was scored based on its relative access to charge sites on the hypothetical peptide ions. Then the distances between exchange sites and these scored carbonyls were used to obtain relative theoretical reactivities of each exchange site which were summed for individual residues to provide a residue score. Finally, the residue scores were scaled based on relative values of surface accessibility using the solvent accessibility surface area (SASA) approach in the VMD software suite. Using these residue scores, the deuterium incorporation was estimated for $[M+3H]^{3+}$ ions using an HDX kinetics model described previously [57]. Briefly, a population of ions (1000) was stepped (1 μs) through a mobility separation (~ 10 ms) and the exchange nature of each site was computed at each step based on the contribution of the residue to the overall rate of exchange for the ions. After stepping all ions through the mobility separation time, the HDX simulation algorithm determined the amount of deuterium incorporation for each residue; this theoretical uptake value is compared to the experimental results below.

Results and Discussion

Peptide Ion Collision Cross Sections

Summing the spectral counts for the $[M+3H]^{3+}$ peptide ions at each mobility selection allows the generation of the t_D distribution shown in Fig. 1 (bottom trace). The distribution is dominated by a feature having a t_D of ~ 8.5 ms. A shoulder, indicating the presence of larger ion conformer types is also observed. With the addition of ~ 0.02 Torr of D_2O, the entire distribution shifts to longer times. The dominant peak is observed to have a t_D of ~ 9.3 ms representing a shift of ~ 0.8 ms. Again, a shoulder of similar intensity is observed at longer t_D values. The shift in the shoulder feature is also observed to be of the same magnitude. That the distribution is similar in the presence and absence of D_2O suggests that the HDX process does not result in structural transformations and it is therefore possible to monitor the reactivities of select ion conformer types. This is similar to results that have been presented for protein ions [61].

From the ion t_D distribution, it is possible to determine the collision cross section of the $[M+3H]^{3+}$ ions. Collision cross sections are determined using Eq. 1 [78]:

$$\Omega = \frac{(18\pi)^{1/2}}{16}\frac{ze}{(k_B T)^{1/2}}\left[\frac{1}{m_I}+\frac{1}{m_B}\right]^{1/2}\frac{t_D E}{L}\frac{760}{P}\frac{T}{273.2}\frac{1}{N} \quad (1)$$

In Eq. 1, ze and k_B are the charge of the ion and Boltzmann's constant, respectively. The variables m_I and m_B are the mass of the ion and the mass of the buffer gas, respectively. E, L, T, and P represent the electric field, the length of the drift tube, and the temperature and pressure of the buffer gas, respectively. Finally, N is the neutral number density at standard temperature and pressure (STP) conditions. Using Eq. 1, the ${}^{He}\Omega_{DT}$ (DT = linear drift tube) is determined to be 424 Å^2 and 464 Å^2 for the prominent feature and shoulder, respectively. These values are larger but similar to those determined for more compact and partially unfolded A-containing peptide conformers (417 Å^2 and 438 Å^2) [34, 77].

A goal in examining the model peptide ions is to begin to determine the degree of similarity in solution- and gas-phase peptide structure in order to better understand ion conformer establishment. A number of studies suggest that a high degree of structure preservation is observed for relatively small proteins [79, 80]. The fate of even smaller peptide ions is less clear. As mentioned above, comparisons of the data reported here for the S-containing peptide are made with those obtained from previous studies of the A-containing peptide because of expected differences in predominant solution conformers. Indeed, CD spectroscopy of the A-containing peptide suggests a high degree of helical character as indicated by the negative bands at ~ 207 and 223 nm as well as the positive band at ~ 190 nm shown in Fig. S1 in the Supplementary Information section. The CD spectrum for the S-containing peptide (Fig. S1 in the Supplementary Information section) shows a very clear difference in predominant solution structure for this peptide where the features indicating α-helix are clearly missing and a broad band at lower wavelengths is indicative of more random coil character.

Because of these differences in solution structure, it is of interest to consider the compact ion conformers for both the S- and A-containing peptides. Notably, the collision cross section of the S-containing peptide is only ~ 1.7% larger than that of the A-containing peptide ion (see above). This occurs even though the molecular weight of the S-containing peptide is ~14.1% larger than that of the comparative peptide. Thus, the overall gas-phase "packing" of the S-containing peptide is more extensive than that of the A-containing peptide. This increased atom density for the S-containing peptide ions offers

the opportunity to determine whether or not distinctive HDX behavior can be observed that would be consistent with such ion structures. Thus for the S-containing peptide, the residue specific deuterium content was examined in detail; the deuterium content was then compared to that of the A-containing peptide and the results are discussed below. Here, it is noted that it was not possible to compare the more elongated conformer of the $[M+3H]^{3+}$ ions as the signal level for the mobility-selected ions was insufficient to obtain ion fragmentation spectra.

Per-residue Deuterium Uptake

Upon introduction of D_2O to the drift tube, the *m/z* of the $[M+3H]^{3+}$ ions shifted to higher values (*m/z*~ 695.4) indicating the incorporation of 20.1 deuteriums (19.9 ± 0.9, on average). Overall there are 48 exchangeable hydrogens (including the three protonation sites). Thus, ~ 41% of the exchangeable hydrogens are observed to undergo exchange. This is similar to the level of deuterium incorporation observed for the A-containing peptide [77]. Therefore, it is useful to consider the amount of deuterium incorporation occurring at the neutral S and A residues. Notably, because the ETD approach used here does not differentiate between side-chain and backbone sites, the question of relative accessibility of different site types for the S residues cannot currently be answered. However, a semi-quantitative comparison of residue accessibility can still be achieved based on the per-residue deuterium content.

To determine the S-residue deuterium content for the gas-phase HDX studies, the more compact $[M+3H]^{3+}$ precursor ions were mobility selected and subjected to ETD both before and after introduction of the D_2O reagent gas. Figure 2a shows the fragmentation spectrum produced for the unlabeled ions. Two strong features are observed at *m/z*~ 688.7 and *m/z*~ 1032.5 and correspond to the $[M+3H]^{3+}$ precursor ions and the charge-reduced, doubly charged ions. Overall, a general lack of low-*m/z* ions is observed in the fragmentation spectrum; dataset features for the z_4 through z_{20} and the c_6 through c_{20} fragment ions are observed. Observed ions used in deuterium content calculations with their associated *m/z* values are provided in Table S1 in the Supplementary Information section. Because many lower *m/z* fragment ions are not observed, the deuterium uptake values for individual amino acid residues have been determined using a combination of *c* and *z* ions. There are two advantages in using both *c* and *z* ions to obtain the uptake values. The first is that nearly complete sequence coverage can be obtained and the second is that a double check of deuterium uptake is provided especially for dataset features of lower intensity.

After undergoing gas-phase HDX, the fragment ions produced by ETD broaden due to an increased number of isotopologues and shift to higher *m/z* values as shown in Fig. 2b. In the case of the *z* ions, by subtracting the z_{i-1} ion from the z_i, the deuterium uptake value for the residue numbered $N-i-1$ can be determined for which N is the number of total peptide residues (21 in this case). For the *c* ions, by measuring the difference between the c_{i-1} and the c_i ions, the deuterium content of the residue number *i* can be calculated. For example, the average *m/z* for the peak corresponding to z_{15} ions is

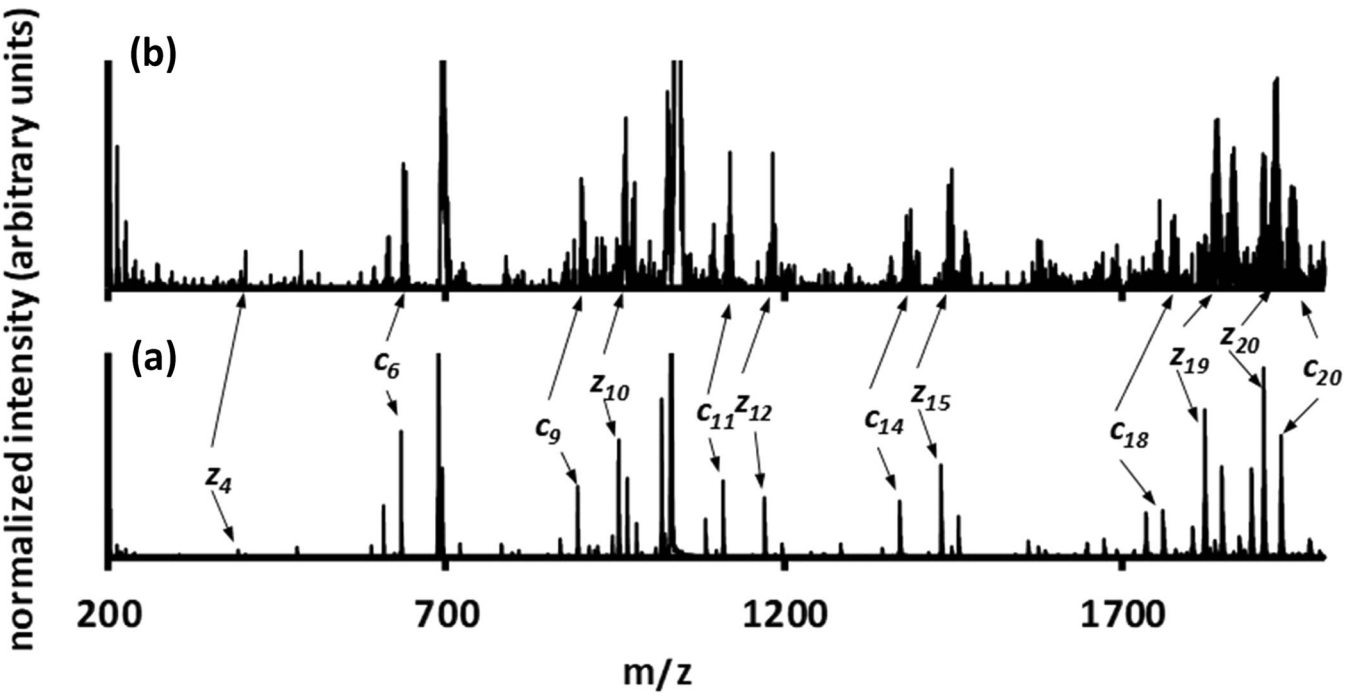

Figure 2. Ion fragmentation spectra obtained upon ETD of the $[M+3H]^{3+}$ ions of the model peptide acetyl-PSSSSKSSSSKSSSSKSSSSK. (**a**) Shows a typical ion fragmentation spectrum for ions that are not exposed to D_2O in the drift tube. (**b**) Shows a typical ion fragmentation spectrum for ions that have been exposed to D_2O in the drift tube. Several *c* and *z* ions are labeled with arrows indicating their location in both spectra

1432.68 and the same peak when D_2O is introduced is *m/z* 1445.40. Thus the deuterium content is calculated to be 12.72. Another example in Fig. 2 is the c_6 ions. In this case, the average *m/z* is 633.70 and the corresponding average *m/z* in the presence of D_2O is 638.78. Here, the deuterium content is 5.08. Table S1 in the Supplementary Information section provides the deuterium uptake values for the amino acid residues obtained from the *z* and *c* ion fragments.

To provide further insight into the determination of deuterium uptake, it is instructive to examine expanded regions of the mass spectra shown in Fig. 2. Fig. S2 in the Supplementary Information section shows expanded regions for three fragment ions. In general, as the fragment ion mass increases, an increased shift to higher *m/z* is observed and a wider isotopic distribution is encountered for ions produced after HDX (Fig. S2 in the Supplementary Information section). For fragment ions produced after HDX, the average *m/z* value is computed by locating the dataset feature edges (typically ≤ 20% peak height) and then computing the weighted average of the isotope peaks between the edges. The average *m/z* of the fragment ion produced prior to introduction of D_2O is then subtracted from this value to obtain the overall *m/z* shift resulting from deuterium incorporation.

S- and A-Residue Deuterium Content Comparison

To investigate whether the per-residue deuterium content reveals differences in relative residue accessibility between the S- and A-containing peptides, the per-residue deuterium content is here compared. As mentioned above, one comparison that is readily available is that of overall HDX efficiency for these resideus. For the S-containing peptide, on average, the number of deuteriums incorporated for all S residues is ~ 9.4 (~ 28.5% of the 33 total available). For the A-containing peptide, a value of ~ 19.5% efficiency (~ 3.3 of 17 available sites), on average, is obtained. The higher efficiency could be reflective of the more compact nature of the S-containing peptide as more exchange sites are in closer proximity to charge sites and deuterium incorporation sites as required by the reaction mechanism [76].

For the reactivity comparisons at the per-residue level, a question arises as to how the evaluation should be performed. For example, the S-containing peptide contains 16 more exchangeable hydrogens due to the side-chain site on the S residues when compared with the A-containing peptide ions. Therefore, a direct comparison of per-residue deuterium content may not provide the simplest representation of the relative accessibility. Thus the S and A deuterium content values are scaled according to their fractional values of the total deuterium incorporated into the neutral residues. K residues are not included in this analysis because, considering the HDX mechanism, different charge site configurations could contribute to the observed differences. Here, rather the interest is in comparing the average differences in accessibility to different regions of the peptide through the use of the S and A residues.

Figure 3 shows the comparison of the deuterium content of the S and A residues on the respective peptide ions. For the A-containing peptide, only four residues show significantly greater accessibility; these are the A4, A5, A19, and A20 residues. For the S-containing peptide, the residues showing significantly increased accessibility are the S2, S9, S10, S13, S15, and S17 residues. Overall, the results suggest a greater accessibility to middle residues for the S-containing peptide ion. This could result from increased charge solvation by the S residues as discussed below. Notably, the relative per-residue deuterium uptake values shown in Fig. 3 exhibit different levels of precision (also shown as independent values in Table S1). This appears to primarily result from variability in determining the peak centers of low-abundance fragment ions. For example, two required fragment ions used to determine the deuterium content for S3 and S18 residues are ~ 40% lower in intensity relative to those used for the S13 and S19 residues. That said, the error levels are consistent with those reported previously [67, 71, 77, 81].

Comparison to Candidate Structures from MD Simulations

The HDX behavior of the S-containing peptide was further considered using MD simulations. To find the best structural type (or types) exhibiting similar exchange site accessibility to the gas-phase conformer type, simulated annealing was conducted for $[M + 3H]^{3+}$ peptide ions using two different charge configurations as well as two different simulation times (see "Experimental"). As shown in Fig. S3 in the Supplementary Information section, the collision cross sections obtained from MD simulations are, for the most part, significantly smaller than the experimental value. An examination of some of these structures, reveals extremely compact ion conformer types with significant charge solvation of the charge sites by the serine residues as shown in Fig. S4 (Supplementary Information section). Indeed, as an indicator of how the MD simulations captured such charge solvation, consider that only 71 of 8000 structures were observed to have collision cross sections within ± 2% of the experimental value for the compact $[M+3H]^{3+}$ ions.

To consider which of the structural types with matching collision cross sections best represented the experimental data, HDX kinetics modeling was employed (see "Experimental" above). Notably, this work does not include the very extensive MD trajectory modeling that was performed previously for the A-containing peptide [34, 35, 77]. Rather, here the MD simulations are only performed to provide an idea of conformer types that could account for the observed HDX accessibility [73]. From HAS scoring and kinetics modeling of the 71 structures, several conformer types appeared to exhibit significant charge solvation by middle residues. Based on the best ability to match the experimental results (see below), one of these ion structures was selected for discussion. This ion structure is shown in Fig. 4C.

The agreement between experimental and theoretical (HDX kinetics modeling) relative deuterium content is shown as a bar graph in Fig. 4A. A number of trends are shown to agree

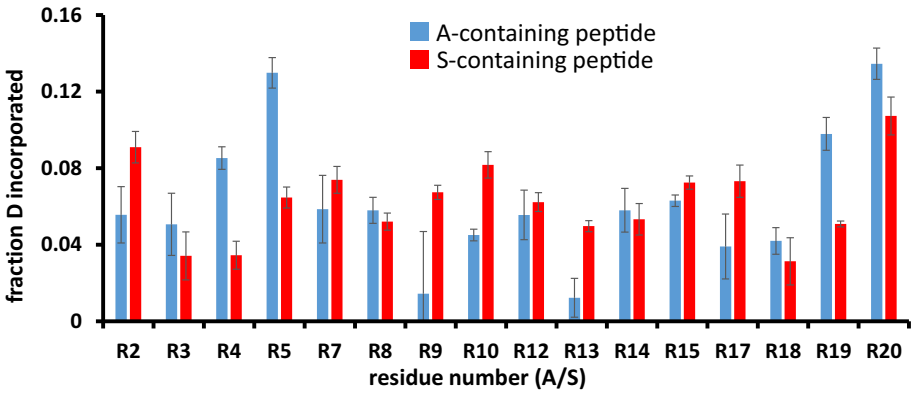

Figure 3. Bar graph showing the fraction of deuterium for S (red bars) and A (blue bars) residues obtained from MS/MS analysis of mobility selected ions. Fractional values are calculated as the ratio of the deuterium content of the specified residue to the total deuterium content from neutral residues for the respective peptides. Error bars are obtained by propagating the error (one standard deviation) of the individual deuterium uptake values

between the experimental and theoretical values. Here, we note that the theory favors sites that are in relative proximity to backbone carbonyls that are in relative proximity to charge sites. A trend captured by the theory for the first ion conformer is the relatively low levels of uptake for S3 and S4 and an increase in uptake for S5 and S7. This is followed by a slight decrease for S8 and then increases for S9 and S10. The model slightly overestimates the deuterium content for S12 to S14. This is followed by relatively good agreement between S15 and S17. The worst agreement is observed at the C-terminal and N-terminal ends for the S2, S18, and S20 residues. Overall, the average percent difference between experiment and theory is observed to be ~27.5% across all S residues.

Figure 4D shows a separate ion conformer for which increased accessibility is observed for the terminal peptide portions relative to middle residues. For example, for this ion conformer there is an increase in estimated deuterium content for the N-terminal residues S3, S4, and S5 with an increase also observed for the C-terminal residues S18, S19, and S20. These increases are offset by decreases in theoretical deuterium content for residues S7 to S14 as well as S17. For this structure, the average percent difference between experiment and theory is ~41.4%.

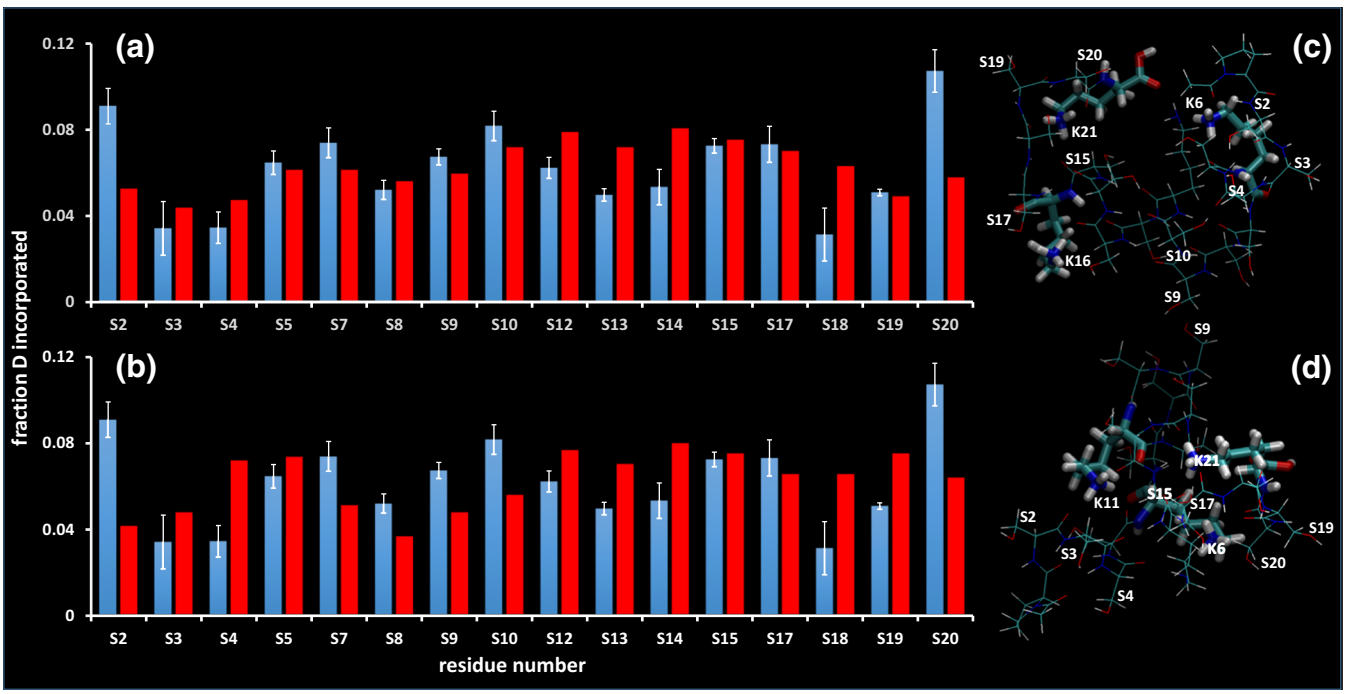

Figure 4. Panel (**a**) shows the comparison of the experimental fraction deuterium incorporated values (blue bars) and the theoretical fraction deuterium incorporated values (red bars) for the ion conformation shown in panel (**c**) of the model peptide acetyl-PSSSSKSSSSKSSSSKSSSSK. Panel (**b**) shows the same comparison for the ion conformation shown in panel (**d**). In panels (**c**) and (**d**), several residues are labeled to demonstrate their relative accessibility for HDX (see text for details)

The differences in the quality of HDX reactivity matching for the ion candidate structures can be described via the HAS scores and the structure images shown in Fig. 4. For the ion structure providing the best HDX reactivity matching, the charge site assignments are K6, K16, and K21 while the charge site assignments for the second ion structure are K6, K11, and K21. One noticeable difference in the structures is that the former ion conformer with its charge arrangement exhibits less charge density. Indeed, the relative Coulomb energy of the former ion conformer is only 69% that of the latter. Thus a more even dispersion of charge throughout the ion conformer is observed. For the first ion conformer (Fig. 4C), the relative increase in theoretical deuterium content would be elevated for the S17 residue due to its hydrogens proximity to the S13 (2.9 Å), S14 (2.1 Å), and S17 (3.6 Å) carbonyls. These carbonyls are highly scored because they are in close proximity to the K21 charge site (all ≤ 1 Å) and the S13 carbonyl is also within 2.5 Å of the K16 charge site. The S15 residue has a large theoretical deuterium uptake as well due to its hydrogens proximity to the K11 (1.9 Å), S12 (3.0 Å), and S14 (3.1 Å) carbonyls. The K11 and S12 carbonyls are scored highly because they are within 3 Å of the K16 and K21 charge sites. In comparison, only one scored carbonyl is positioned at ≤ 4 Å from the S19 hydrogens. The increased theoretical deuterium uptake for the S10 to the S14 sites results from the fact that these residues fall between the K6 and K16 charge sites and there is a significant compaction of this portion of the ion such that exchange sites are in close proximity to a greater number of carbonyl sites. For example, the S10 residue has hydrogens that are within 1.8 Å and 2.9 Å of scored carbonyls on the S4 and S7 residues. Additionally, labile hydrogens are ≤ 4 Å of scored carbonyls on the S8 and S9 residues. These scored carbonyls are in closer proximity to the K6 charge site. Finally, although the S2, S3, and S4 residues are in relative proximity to the K6 charge site, there is a decreased number of close carbonyl sites. For example, for hydrogens on the S2 residue, only the S2 carbonyl is within ≤ 4 Å.

For the ion conformation presenting decreased agreement in theoretical and experimental deuterium content (Fig. 4), the decrease at S2 results from the placement of this residue further away from charge sites. This is evident from the fact that the only carbonyl sites within 4 Å of any hydrogen on the S2 residue are the N-terminal acetyl group and the P1 residue and both of these carbonyls are not highly scored due to their distance to charge sites. Decreases in middle residues S9 and S10 can be seen to result from the placement of these residues further away from charge sites and scored carbonyl sites. For example, hydrogens on the S10 residue only encounter the S8 carbonyl at a distance that is ≤ 4 Å. Finally, the increased theoretical deuterium content at the C-terminal residues (S18, S19, and S20) results from the fact that these residues are in close proximity to the K6 and K21 charge sites as well as a number of carbonyl sites. For example, the hydrogens on the S19 residue are within 1.5 Å and 2.5 Å of the scored carbonyls on the S18 and S19 residues. These carbonyls are scored highly as they are 0.5 Å and 1.7 Å from the K21 charge site. Additionally, the latter carbonyl is also within 5.7 Å of the K6 and K11 residues. As shown in Fig. 4, the structure exhibiting the decreased HDX reactivity match appears to position the S4 and S5 residues such that they would not exhibit greater accessibility as determined by the HAS approach. However, upon rotation of the ion structure, it becomes apparent that the exchangeable hydrogens on the S4 and S5 residues are near a number of highly scored carbonyl sites as shown in Fig. S5 in the Supplementary Information section. Indeed, the hydrogens on these residues are ≤ 2 Å from the N-terminal acetyl group carbonyl and the P1 carbonyl.

It is instructive to consider the type of ion structure that would be required to result in increased exchange of the S2 and S20 residues as is observed experimentally (Fig. 4). One consideration is that more compact structures in which the N-terminal and C-terminal ends turn back toward the middle residues would provide increased HAS scores for these residues. Fig. S6 in the Supplementary Information section shows a compact ion structure ($^{He}\Omega_{DT}$ = 363.0 Å^2) for which HAS scoring and HDX kinetics modeling was performed. The relative deuterium incorporation levels for several residues are also shown in Fig. S6. Notably, the value for the S20 residue is the largest of all residues and that of S2 is among the largest values as well. Additionally, the deuterium incorporation values for the neighboring S4 and S18 residues are among the lowest. These results are similar to what is observed experimentally for N- and C-terminal residues (Figs. 3 and 4). The high value for the S2 residue results from the fact that a N-terminal bend positions this residue such that the S2 backbone hydrogen is in relatively close proximity of the acetyl carbonyl (3.3 Å), the P1 carbonyl (3.1 Å), and the S2 carbonyl (2.1 Å). These carbonyl sites also have relatively high scores as they are located near the K6 charge site. The side-chain hydrogen of S2 is located near (1.7 Å) the S10 carbonyl which is one of the highest scoring carbonyl sites being near multiple charge sites. In contrast, the backbone hydrogen and the side-chain hydrogen of the S4 residue are not within 3 and 4 Å, respectively, of any scored carbonyl. For the S20 residue, hydrogens are in close proximity to the highly scored carbonyls on S19 (3.1 Å) and S8 (2.0 Å). The S18 residue hydrogens are not within 3 Å of any scored carbonyl.

It is necessary to present a note of caution regarding the comparisons between theoretical and experimental deuterium uptake here. Such comparisons are not intended to be definitive as they do not consider ion conformer dynamics or the possible contribution by multiple ion conformers with different charge site configurations. As mentioned above, the failings of the approach are especially obvious in the inability of either ion structure to account for the increased deuterium content of the S2 and S20 residues observed experimentally. The improved matching of HAS scores with experimental values for these residues when using a far too compact ion structure is intriguing. For example, such analysis may suggest that multiple ion conformer types comprise the mobility selection and a portion of these contain bends at either the N-terminal or the C-terminal end with the other end extended (in order to exhibit the correct cross section). That said, the comparisons are useful insofar as they demonstrate conformer types exhibiting specific charge solvation that could account for the observed differences in relative deuterium content of specific peptide regions. Additionally, such comparisons represent the foundational work that will be extended to exhaustive

MD simulations that do account for conformer dynamics as well as the presence of different conformer types. In future works, such simulations will be conducted in the gas and solution phases as was performed for the A-containing peptide [34, 35] and the results will be compared with regard to the preferred types of structure formed for the different ions.

Conclusions

IMS-HDX-MS/MS measurements coupled with MD simulations have been used to gain insight into the behavior of $[M+3H]^{3+}$ ions of the model peptide acetyl-PSSSSKSSSSKSSSSKSSSSK. From the IMS measurements a dominant, compact ion conformer is observed. In comparison to the same ions for the model peptide acetyl-PAAAAKAAAAKAAAAKAAAAK, the S-containing peptide is observed to be relatively more compact. This may be somewhat expected as CD spectroscopy suggests that the former peptide exhibits more random coil nature while the A-containing peptide exhibits significantly more α-helical character. In addition to, and likely attributed to, the increased compactness, the S-containing peptide shows increased accessibility of interior residues to gas-phase HDX. MD simulations suggest that ion conformers demonstrating specific, relatively disperse charge solvation by interior residues could account for the observed HDX behavior of the $[M+3H]^{3+}$ ions.

The disparity in hypothetical and experimental deuterium uptake suggests the need for highly extensive MD simulations to better understand the contributions of ion structure dynamics as well as contributions from multiple ion conformers. This limitation was also encountered for the A-containing peptide where exhaustive gas-phase and ESI droplet simulations have been conducted to better fit the experimental data [34, 35]. Thus, in order to gain insight into the ion structures resulting from very different solution structures, it will be necessary, in future studies, to conduct these same exhaustive analyses where a convergence between gas-phase ion structures and those emerging from ESI droplets is obtained. With these structures it will be possible to compare the major differences in structures arising from the S- and A-containing peptides. The comparison of such predominant structures could provide information about the degree of preservation of secondary structure for these smaller biomolecules and could thus help with our understanding of the process of gas-phase ion structure establishment.

Acknowledgements

We are grateful for financial support from the National Institutes of Health (R01GM114494).

References

1. Pauling, L., Corey, R.B.: Two hydrogen-bonded spiral configurations of the polypeptide chain. J. Am. Chem. Soc. **72**(5349–5349), (1950)
2. Pace, C.N., Scholtz, J.M.: A helix propensity scale based on experimental studies of peptides and proteins. Biophys. J. **75**, 422–427 (1998)
3. Davies, D.R.: A correlation between amino acid composition and protein structure. J. Mol. Biol. **9**, 605–609 (1964)
4. Guzzo, A.V.: The influence of amino acid sequence on protein structure. Biophys. J. **5**, 809–822 (1965)
5. Prothero, J.W.: Correlation between the distribution of amino acids and alpha helices. Biophys. J. **6**, 367–370 (1966)
6. Cook, D.A.: The relation between amino acid sequence and protein conformation. J. Mol. Biol. **29**, 167–171 (1967)
7. Ptitsyn, O.B.: Statistical analysis of the distribution of amino acid residues among helical and non-helical regions in globular proteins. J. Mol. Biol. **42**, 501–510 (1969)
8. Chou, P.Y., Fasman, G.D.: Conformational parameters for amino acids in helical, β-sheet, and random coil regions calculated from proteins. Biochemistry. **13**, 211–222 (1974)
9. Defay, T., Cohen, F.E.: Evaluation of current techniques for ab initio protein structure prediction. Proteins. **23**, 431–445 (1995)
10. Frishman, D., Argos, P.: The future of protein secondary structure prediction accuracy. Fold. Des. **2**, 159–162 (1997)
11. Creamer, T.P., Rose, G.D.: Alpha-helix-forming propensities in peptides and proteins. Proteins. **19**, 85–97 (1994)
12. Horovitz, A., Matthews, J.M., Fersht, A.R.: Alpha-helix stability in proteins. II. Factors that influence stability at an internal position. J. Mol. Biol. **227**, 560–568 (1992)
13. Krause, E., Bienert, M., Schmieder, P., Wenschuh, H.: The helix-destabilizing propensity scale of d-amino acids: the influence of side chain steric effects. J. Am. Chem. Soc. **122**, 4865–4870 (2000)
14. Towse, C.-L., Hopping, G., Vulovic, I., Daggett, V.: Nature versus design: the conformational propensities of d-amino acids and the importance of side chain chirality. Protein Eng. Des. Sel. **27**, 447–455 (2014)
15. Manjasetty, B.A., Büssow, K., Panjikar, S., Turnbull, A.P.: Current methods in structural proteomics and its applications in biological sciences. 3 Biotech. **2**, 89–113 (2012)
16. Berman, H.M., Westbrook, J., Feng, Z., Gilliland, G., Bhat, T.N., Weissig, H., Shindyalov, I.N., Bourne, P.E.: The Protein Data Bank. Nucleic Acids Res. **28**, 235–242 (2000)
17. Petrey, D., Honig, B.: Protein structure prediction: inroads to biology. Mol. Cell. **20**, 811–819 (2005)
18. Qu, X.T., Swanson, R., Day, R., Tsai, J.: A guide to template based structure prediction. Curr. Protein Pept. Sci. **10**, 270–285 (2009)
19. Forrest, L.R., Tang, C.L., Honig, B.: On the accuracy of homology modeling and sequence alignment methods applied to membrane proteins. Biophys. J. **91**, 508–517 (2006)
20. Dorn, M., MB, E.S., Buriol, L.S., Lamb, L.C.: Three-dimensional protein structure prediction: methods and computational strategies. Comput. Biol. Chem. **53pb**, 251–276 (2014)
21. Li, B., Fooksa, M., Heinze, S., Meiler, J.: Finding the needle in the haystack: towards solving the protein-folding problem computationally. Crit. Rev. Biochem. Mol. Biol. **53**, 1–28 (2018)
22. Tian, X.Y., Chen, D.Z., Gao, J.: An overview on protein fold classification via machine learning approach. Curr Proteomics. **15**, 85–98 (2018)
23. Almeida, J.G., Preto, A.J., Koukos, P.I., Bonvin, A., Moreira, I.S.: Membrane proteins structures: a review on computational modeling tools. Biochimica Et Biophysica Acta-Biomembranes. **1859**, 2021–2039 (2017)
24. Uversky, V.N.: What does it mean to be natively unfolded? Eur. J. Biochem. **269**, 2–12 (2002)
25. Chatterjee, A., Kumar, A., Chugh, J., Srivastava, S., Bhavesh, N.S., Hosur, R.V.: NMR of unfolded proteins. J. Chem. Sci. **117**, 3–21 (2005)
26. Fink, A.L.: Natively unfolded proteins. Curr. Opin. Struct. Biol. **15**, 35–41 (2005)
27. Bracken, C., Iakoucheva, L.M., Rorner, P.R., Dunker, A.K.: Combining prediction, computation and experiment for the characterization of protein disorder. Curr. Opin. Struct. Biol. **14**, 570–576 (2004)
28. Meng, F.C., Uversky, V.N., Kurgan, L.: Comprehensive review of methods for prediction of intrinsic disorder and its molecular functions. Cell. Mol. Life Sci. **74**, 3069–3090 (2017)

29. Hicks, R.P.: Recent advances in NMR: expanding its role in rational drug design. Curr. Med. Chem. **8**, 627–650 (2001)
30. Pierson, N.A., Chen, L., Valentine, S.J., Russell, D.H., Clemmer, D.E.: Number of solution states of bradykinin from ion mobility and mass spectrometry measurements. J. Am. Chem. Soc. **133**, 13810–13813 (2011)
31. Pierson, N.A., Valentine, S.J., Clemmer, D.E.: Evidence for a quasi-equilibrium distribution of states for bradykinin M+3H (3+) ions in the gas phase. J. Phys. Chem. B. **114**, 7777–7783 (2010)
32. Shi, H.L., Pierson, N.A., Valentine, S.J., Clemmer, D.E.: Conformation types of ubiquitin M+8H (8+) ions from water:methanol solutions: evidence for the N and a states in aqueous solution. J. Phys. Chem. B. **116**, 3344–3352 (2012)
33. Khakinejad, M., Ghassabi Kondalaji, S., Tafreshian, A., Valentine, S.J.: Comprehensive gas-phase peptide ion structure studies using ion mobility techniques: part 2. Gas-phase hydrogen/deuterium exchange for ion population estimation. Journal of The American Society for Mass Spectrometry. 1–11 (2017)
34. Ghassabi Kondalaji, S., Khakinejad, M., Tafreshian, A., S, J.V.: Comprehensive peptide ion structure studies using ion mobility techniques: part 1. An advanced protocol for molecular dynamics simulations and collision cross-section calculation. J. Am. Soc. Mass Spectrom. **28**, 947–959 (2017)
35. Ghassabi Kondalaji, S.K.M, Valentine, S. J.: Comprehensive peptide ion structure studies using ion mobility techniques: part 3. Relating solution-phase to gas-phase structures. Journal of the American Society for Mass Spectrometry. J. Am. Soc. Mass Spectrom. **29**, 1665–1677 (2018)
36. Chakrabartty, A., Kortemme, T., Baldwin, R.L.: Helix propensities of the amino acids measured in alanine-based peptides without helix-stabilizing side-chain interactions. Protein Sci. **3**, 843–852 (1994)
37. Palencar, P., Bleha, T.: Molecular dynamics simulations of the folding of poly (alanine) peptides. J. Mol. Model. **17**, 2367–2374 (2011)
38. Hudgins, R.R., Ratner, M.A., Jarrold, M.F.: Design of helices that are stable in vacuo. J. Am. Chem. Soc. **120**, 12974–12975 (1998)
39. Straus, R.N., Jockusch, R.A.: Probing the gaseous structure of a beta-hairpin peptide with H/D exchange and electron capture dissociation. J. Am. Soc. Mass Spectrom. **28**, 358–369 (2017)
40. Pan, J.X., Heath, B.L., Jockusch, R.A., Konermann, L.: Structural interrogation of electrosprayed peptide ions by gas-phase H/D exchange and electron capture dissociation mass spectrometry. Anal. Chem. **84**, 373–378 (2012)
41. Ballesteros, J.A., Deupi, X., Olivella, M., Haaksma, E.E., Pardo, L.: Serine and threonine residues bend alpha-helices in the chi(1) = g(-) conformation. Biophys. J. **79**, 2754–2760 (2000)
42. Imai, K., Mitaku, S.: Mechanisms of secondary structure breakers in soluble proteins. Biophysics. **1**, 55–65 (2005)
43. Konermann, L., Ahadi, E., Rodriguez, A.D., Vahidi, S.: Unraveling the mechanism of electrospray ionization. Anal. Chem. **85**, 2–9 (2013)
44. Kim, D., Wagner, N., Wooding, K., Clemmer, D.E., Russell, D.H.: Ions from solution to the gas phase: a molecular dynamics simulation of the structural evolution of substance P during desolvation of charged nanodroplets generated by electrospray ionization. J. Am. Chem. Soc. **139**, 2981–2988 (2017)
45. Glaskin, R.S., Khatri, K., Wang, Q., Zaia, J., Costello, C.E.: Construction of a database of collision cross section values for glycopeptides, glycans, and peptides determined by IM-MS. Anal. Chem. **89**, 4452–4460 (2017)
46. Soper-Hopper, M.T., Petrov, A.S., Howard, J.N., Yu, S.S., Forsythe, J.G., Grover, M.A., Fernández, F.M.: Collision cross section predictions using 2-dimensional molecular descriptors. Chem. Commun. **53**, 7624–7627 (2017)
47. Zheng, X.Y., Deng, L.L., Baker, E.S., Ibrahim, Y.M., Petyuk, V.A., Smith, R.D.: Distinguishing D- and L-aspartic and isoaspartic acids in amyloid beta peptides with ultrahigh resolution ion mobility spectrometry. Chem. Commun. **53**, 7913–7916 (2017)
48. Daly, S., MacAleese, L., Dugourd, P., Chirot, F.: Combining structural probes in the gas phase - ion mobility-resolved action-FRET. J. Am. Soc. Mass Spectrom. **29**, 133–139 (2018)
49. Benigni, P., Porter, J., Ridgeway, M.E., Park, M.A., Fernandez-Lima, F.: Increasing analytical separation and duty cycle with nonlinear analytical mobility scan functions in TIMS-FT-ICR MS. Anal. Chem. **90**, 2446–2450 (2018)
50. Stocks, B.B., Melanson, J.E.: In-source reduction of disulfide-bonded peptides monitored by ion mobility mass spectrometry. J. Am. Soc. Mass Spectrom. **29**, 742–751 (2018)
51. Heo, C.E., Choi, T.S., Kim, H.I.: Competitive homo- and hetero- self-assembly of amyloid-beta 1-42 and 1-40 in the early stage of fibrillation. Int. J. Mass Spectrom. **428**, 15–21 (2018)
52. Fouque, K.J.D., Garabedian, A., Porter, J., Baird, M., Pang, X.Q., Williams, T.D., Li, L., Shvartsburg, A., Fernandez-Lima, F.: Fast and effective ion mobility-mass spectrometry separation of D-amino-acid-containing peptides. Anal. Chem. **89**, 11787–11794 (2017)
53. Lee, J.W., Lee, H.H.L., Davidson, K.L., Bush, M.F., Kim, H.I.: Structural characterization of small molecular ions by ion mobility mass spectrometry in nitrogen drift gas: improving the accuracy of trajectory method calculations. Analyst. **143**, 1786–1796 (2018)
54. Majuta, S.N., Maleki, H., Kiani Karanji, A., Attanyake, K., Loch, E., Valentine, S.J.: Magnifying ion mobility spectrometry-mass spectrometry measurements for biomolecular structure studies. Curr. Opin. Chem. Biol. **42**, 101–110 (2018)
55. Clowers, B.H., Hill, H.H.: Mass analysis of mobility-selected ion populations using dual gate, ion mobility, quadrupole ion trap mass spectrometry. Anal. Chem. **77**, 5877–5885 (2005)
56. Zucker, S.M., Lee, S., Webber, N., Valentine, S.J., Reilly, J.P., Clemmer, D.E.: An ion mobility/ion trap/photodissociation instrument for characterization of ion structure. J. Am. Soc. Mass Spectrom. **22**, 1477–1485 (2011)
57. Khakinejad, M., Kondalaji, S.G., Maleki, H., Arndt, J.R., Donohoe, G.C., Valentine, S.J.: Combining ion mobility spectrometry with hydrogen-deuterium exchange and top-down MS for peptide ion structure analysis. J. Am. Soc. Mass Spectrom. **25**, 2103–2115 (2014)
58. Donohoe, G.C., Maleki, H., Arndt, J.R., Khakinejad, M., Yi, J.H., McBride, C., Nurkiewicz, T.R., Valentine, S.J.: A new ion mobility-linear ion trap instrument for complex mixture analysis. Anal. Chem. **86**, 8121–8128 (2014)
59. Wood, T.D., Chorush, R.A., Wampler, F.M., Little, D.P., Oconnor, P.B., McLafferty, F.W.: Gas-phase folding and unfolding of cytochrome-c cations. Proc. Natl. Acad. Sci. U. S. A. **92**, 2451–2454 (1995)
60. Suckau, D., Shi, Y., Beu, S.C., Senko, M.W., Quinn, J.P., Wampler III, F.M., McLafferty, F.W.: Coexisting stable conformations of gaseous protein ions. Proc. Natl. Acad. Sci. U. S. A. **90**, 790–793 (1993)
61. Valentine, S.J., Clemmer, D.E.: H/D exchange levels of shape-resolved cytochrome c conformers in the gas phase. J. Am. Chem. Soc. **119**, 3558–3566 (1997)
62. Wyttenbach, T., Bowers, M.T.: Gas phase conformations of biological molecules: the hydrogen/deuterium exchange mechanism. J. Am. Soc. Mass Spectrom. **10**, 9–14 (1999)
63. Freitas, M.A., Hendrickson, C.L., Emmett, M.R., Marshall, A.G.: Gas-phase bovine ubiquitin cation conformations resolved by gas-phase hydrogen/deuterium exchange rate and extent. Int. J. Mass Spectrom. **185**, 565–575 (1999)
64. Chipuk, J.E., Brodbelt, J.S.: Investigation of the gas-phase hydrogen/deuterium exchange behavior of aromatic dicarboxylic acids in a quadrupole ion trap. Int. J. Mass Spectrom. **267**, 98–108 (2007)
65. Zhang, J.M., Brodbelt, J.S.: Gas-phase hydrogen/deuterium exchange and conformations of deprotonated flavonoids and gas-phase acidities of flavonoids. J. Am. Chem. Soc. **126**, 5906–5919 (2004)
66. Gabelica, V., Rosu, F., Witt, M., Baykut, G., De Pauw, E.: Fast gas-phase hydrogen/deuterium exchange observed for a DNA G-quadruplex. Rapid Commun. Mass Spectrom. **19**, 201–208 (2005)
67. Mistarz, U.H., Brown, J.M., Haselmann, K.F., Rand, K.D.: Simple setup for gas-phase H/D exchange mass spectrometry coupled to electron transfer dissociation and ion mobility for analysis of polypeptide structure on a liquid chromatographic time scale. Anal. Chem. **86**, 11868–11876 (2014)
68. Rand, K.D., Zehl, M., Jensen, O.N., Jorgensen, T.J.: Loss of ammonia during electron-transfer dissociation of deuterated peptides as an inherent gauge of gas-phase hydrogen scrambling. Anal. Chem. **82**, 9755–9762 (2010)
69. Rand, K.D., Adams, C.M., Zubarev, R.A., Jorgensen, T.J.D.: Electron capture dissociation proceeds with a low degree of intramolecular migration of peptide amide hydrogens. J. Am. Chem. Soc. **130**, 1341–1349 (2008)
70. Syka, J.E.P., Coon, J.J., Schroeder, M.J., Shabanowitz, J., Hunt, D.F.: Peptide and protein sequence analysis by electron transfer dissociation mass spectrometry. Proc. Natl. Acad. Sci. U. S. A. **101**, 9528–9533 (2004)
71. Khakinejad, M., Kondalaji, S.G., Tafreshian, A., Valentine, S.J.: Gas-phase hydrogen-deuterium exchange labeling of select peptide ion

conformer types: a per-residue kinetics analysis. J Am Soc Mass Spectrom. (2015)
72. Donohoe, G.C., Arndt, J.R., Valentine, S.J.: Online deuterium hydrogen exchange and protein digestion coupled with ion mobility spectrometry and tandem mass spectrometry. Anal. Chem. **87**, 5247–5254 (2015)
73. Khakinejad, M., Kondalaji, S.G., Tafreshian, A., Valentine, S.J.: Gas-phase hydrogen-deuterium exchange labeling of select peptide ion conformer types: a per-residue kinetics analysis. J. Am. Soc. Mass Spectrom. **26**, 1115–1127 (2015)
74. Jarrold, M.F.: Mobcal, A program to calculate mobilities. 2/10/2014-2/18/2016. Available from: http://www.indiana.edu/~nano/software.html. Accessed 1 June 2014
75. Mesleh, M.F., Hunter, J.M., Shvartsburg, A.A., Schatz, G.C., Jarrold, M.F.: Structural information from ion mobility measurements: effects of the long-range potential. J. Phys. Chem. **100**, 16082–16086 (1996)
76. Campbell, S., Rodgers, M.T., Marzluff, E.M., Beauchamp, J.L.: Deuterium exchange reactions as a probe of biomolecule structure. Fundamental studies of cas phase H/D exchange reactions of protonated glycine oligomers with D2O, CD3OD, CD3CO2D, and ND3. J. Am. Chem. Soc. **117**, 12840–12854 (1995)
77. Khakinejad, M., Ghassabi Kondalaji, S., Tafreshian, A., Valentine, S.J.: Comprehensive gas-phase peptide ion structure studies using ion mobility techniques: part 2. Gas-phase hydrogen/deuterium exchange for ion population estimation. J. Am. Soc. Mass Spectrom. **28**, 960–970 (2017)
78. Mason, E.A.M., E. W. Wiley, New York (1988)
79. Seo, J., Hoffmann, W., Warnke, S., Bowers, M.T., Pagel, K., von Helden, G.: Retention of native protein structures in the absence of solvent: a coupled ion mobility and spectroscopic study. Angew. Chem. Int. Ed. **55**, 14173–14176 (2016)
80. Wyttenbach, T., Bowers, M.T.: Structural stability from solution to the gas phase: native solution structure of ubiquitin survives analysis in a solvent-free ion mobility-mass spectrometry environment. J. Phys. Chem. B. **115**, 12266–12275 (2011)
81. Rand, K.D., Pringle, S.D., Morris, M., Brown, J.M.: Site-specific analysis of gas-phase hydrogen/deuterium exchange of peptides and proteins by electron transfer dissociation. Anal. Chem. **84**, 1931–1940 (2012)